nanomaterials

MDPI

Article

Bilayer $MoSe_2/HfS_2$ Nanocomposite as a Potential Visible-Light-Driven Z-Scheme Photocatalyst

Biao Wang [1,*], Xiaotian Wang [1], Peng Wang [1], Tie Yang [1], Hongkuan Yuan [1], Guangzhao Wang [2] and Hong Chen [1,3,*]

1 School of Physical Science and Technology, Southwest University, Chongqing 400715, China; wangxt45@126.com (X.W.); wangpeng9@swu.edu.cn (P.W.); yangtie@swu.edu.cn (T.Y.); yhk10@swu.edu.cn (H.Y.)

2 School of Electronic Information Engineering, Key Laboratory of Extraordinary Bond Engineering and Advanced Materials Technology of Chongqing, Yangtze Normal University, Chongqing 408100, China; wangyan6930@yznu.edu.cn

3 Key Laboratory of Luminescent and Real-Time Analytical Chemistry, Ministry of Education, College of Chemistry and Chemical Engineering, Southwest University, Chongqing 400715, China

* Correspondence: wbfxz@swu.edu.cn (B.W.); chenh@swu.edu.cn (H.C.)

Received: 29 October 2019; Accepted: 25 November 2019; Published: 28 November 2019

Abstract: Visible-light-driven photocatalytic overall water splitting is deemed to be an ideal way to generate clean and renewable energy. The direct Z-scheme photocatalytic systems, which can realize the effective separation of photoinduced carriers and possess outstanding redox ability, have attracted a huge amount of interest. In this work, we have studied the photocatalytic performance of the bilayer $MoSe_2/HfS_2$ van der Waals (vdW) heterojunction following the direct Z-scheme mechanism by employing the hybrid density functional theory. Our calculated results show that the HfS_2 and $MoSe_2$ single layers in this heterojunction are used for the oxygen evolution reaction (OER) and hydrogen evolution reaction (HER), respectively. The charge transfer between the two layers brought about an internal electric field pointing from the $MoSe_2$ layer to the HfS_2 slab, which can accelerate the separation of the photoinduced electron–hole pairs and support the Z-scheme electron migration near the interface. Excitingly, the optical absorption intensity of the $MoSe_2/HfS_2$ heterojunction is enhanced in the visible and infrared region. As a result, these results reveal that the $MoSe_2/HfS_2$ heterojunction is a promising direct Z-scheme photocatalyst for photocatalytic overall water splitting.

Keywords: $MoSe_2/HfS_2$; direct Z-scheme; photocatalytic water splitting; hybrid functional study

1. Introduction

In order to set up a sustainable society, photocatalytic water splitting for hydrogen production has been deemed as an effective route to solve the problems of environmental pollution and energy shortage [1]. Owing to the groundbreaking work by Honda and Fujishima in 1972 [2], a variety of semiconductor materials have been extensively investigated to explore high-performance photocatalysts for water decomposition [3–7]. However, a majority of one-component photocatalysts, such as TiO_2 and ZnO, can only utilize a small amount of the solar energy and the lifetimes of photoinduced electron–hole pairs in these materials are short, which leads to the problem that the photocatalytic efficiency is low and hampers their future applications [8,9]. For the sake of overcoming these disadvantages, many researchers have found that the construction of heterostructures, which are composed of different materials and can supply much greater control of the electronic and optical properties, is able to effectively enhance the catalytic activity [10–15].

In particular, great expectations have been placed on the Z-scheme photocatalytic mechanism—which includes two-step excitation and is illuminated by natural photosynthesis

in plants [16]—for improving the utilization efficiency of sunlight [17–24]. Generally speaking, the Z-scheme photocatalytic system is made up of three parts: Catalysts for the hydrogen evolution reaction (HER), oxygen evolution reaction (OER), and the redox mediator for carrier migration [25]. According to this mechanism, although the isolated components cannot accomplish overall water splitting, the combined systems can decompose water into hydrogen and oxygen, which can broaden the scope of the promising photocatalysts. Moreover, the Z-scheme photocatalytic composites possess strong redox abilities and can benefit the separation of photogenerated carriers because of the occurrence of HER and OER on different layers [26]. Nevertheless, the redox mediators in Z-scheme photocatalysts may induce undesired back reactions and seriously affect the photocatalytic performance [27]. Z-scheme systems without mediators, which are named as direct Z-scheme photocatalysts, can avoid the problems caused by mediators and are easier to experimentally fabricate owing to their simpler structures. Therefore, the direct Z-scheme systems have been extensively studied [28–32].

Recently, various two-dimensional (2D) materials, such as graphene [33], g-C_3N_4 [34], $MoSe_2$ [35], and HfS_2 [36] have been predicated and fabricated [37]. Owing to the maximized specific surface area, high charge migration, and unique electronic properties derived from the quantum confinement effect, 2D materials and related heterostructures have attracted much attention as high-performance photocatalysts for water [38–40]. However, being limited by the band edge positions, the isolated $MoSe_2$ and HfS_2 monolayers can only be used for the HER and OER [41,42], respectively. Fortunately, the band edge positions of $MoSe_2$ and HfS_2 single layers present staggered-type (type II) band alignment characteristics [43,44], which are beneficial for establishing the Z-scheme composites. Therefore, we have designed $MoSe_2$/HfS_2 bilayer nanocomposites and studied their geometric structures, band structures, density of states, charge transfer, stress effect, and optical properties by employing the hybrid density functional theory.

2. Computational Method

In this work, all of the density functional theory calculations were employed with the Vienna ab initio simulation package (VASP) [45]. The frozen-core projector augmented wave (PAW) was used to describe the interaction between the core and valence electrons [46,47]. The generalized gradient approximation (GGA) [48] of the Perdew–Burke–Ernzerhof (PBE) exchange correlation functional [49] was adopted. The charge redistribution in the $MoSe_2$/HfS_2 heterojunction was considered by calculating the dipole correction [50]. For the sake of avoiding the undervaluation of bandgaps calculated by the PBE method, the electronic and optical properties of these referred materials were calculated by the Heyd–Scuseria–Ernzerhof (HSE) hybrid functional by adding a part of the exact exchange interaction [51]. An exact exchange contribution of 0.25 was used in this study. The long-range van der Waals (vdW) interaction of heterojunctions was described by the Grimmes DFT-D3 method [52]. A Γ-centered 7 × 7 × 1 K-point was used to sample the 2D Brillouin Zone [53]. The cutoff energy was set as 500 eV. The convergence criteria were less than 10^{-5} eV for total energy and 0.01 eV/Å for Hellman–Feynman force on each atom, respectively. A vacuum space of 20 Å was inserted perpendicular to the layers to separate the neighboring slabs of heterojunctions. The band edge positions of 2D materials were calculated by subtracting vacuum levels, which were obtained by averaging the values in the LOCPOT file; they were then applied for measuring the absolute positions of energy bands.

3. Results and Discussion

3.1. Structural Stability

In this study, we chose the hexagonal $MoSe_2$ and HfS_2 monolayers, which are able to fit each other well. After the structural optimization, the lattice constants of $MoSe_2$ and HfS_2 single layers were 3.30 Å and 3.61 Å, respectively, which agree with the previous values [54]. Due to the small lattice mismatch of these single layers, we designed a heterojunction composed of 2 × 2 $MoSe_2$ and HfS_2

supercells. In order to probe into the steadiest stacked pattern, we studied various configurations. The steadiest configuration of the $MoSe_2/HfS_2$ heterojunction, whose equilibrium structure is presented in Figure 1, will be studied in the subsequent parts.

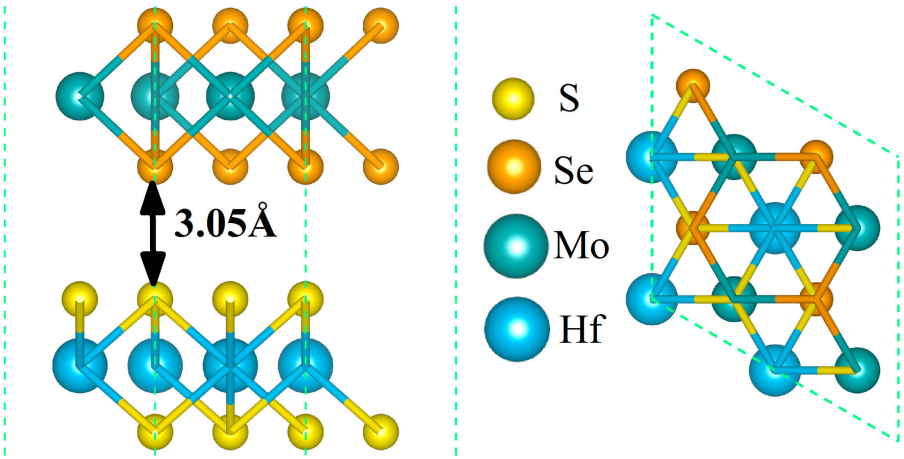

Figure 1. The equilibrium structure of the $MoSe_2/HfS_2$ nanocomposite. Orange and peacock-blue balls signify Se and Mo atoms in the $MoSe_2$ monolayer; yellow and dodger-blue balls symbolize S and Hf atoms in the HfS_2 single layer, respectively. The side view (**a**) and top view (**b**) of this heterojunction.

In addition, the interlayer spacing of the $MoSe_2/HfS_2$ heterobilayer was 3.05 Å, as displayed in Figure 1, which refers to the vertical distance from the nearest S atoms of the HfS_2 layer to the Se atoms of the $MoSe_2$ layer. This vertical separation between two layers is a typical vdW equilibrium distance, which is in accord with other 2D vdW heterostructures [11,44]. Thus, it was necessary to add the vdW corrections into our computation. The binding energy (E_b) of the $MoSe_2/HfS_2$ heterojunction can be defined as this equation: $E_b = E_{MoSe2/HfS2} - E_{MoSe2} - E_{HfS2}$, where $E_{MoSe2/HfS2}$, E_{MoSe2}, and E_{HfS2} stand for the total energy of this heterostructure, isolated $MoSe_2$, and HfS_2 monolayers, respectively. After calculations, the bound energy of the steadiest configuration of the $MoSe_2/HfS_2$ heterojunction is –0.27 eV, which means that this composite is stable.

3.2. Electronic Properties

The band structures of related materials were calculated by employing the hybrid functional. As presented in Table 1, the bandgaps of $MoSe_2$ and HfS_2 monolayers were 2.02 and 1.99 eV, respectively, which are consistent with the previous calculations [54] and mean that the two layers can both utilize the visible light irradiation. Moreover, the valence band maximum (VBM) and conduction band minimum (CBM) of the HfS_2 monolayer were both lower than those of $MoSe_2$ single layer, which indicates that $MoSe_2/HfS_2$ heterobilayer can form a type II heterostructure. As we all know, all of the direct Z-scheme systems have a typical type II band alignment structure [26]. Therefore, the $MoSe_2/HfS_2$ heterojunction can form a direct Z-scheme photocatalyst.

Table 1. Bandgaps and band edge positions of the related nanosheets.

Structure	E_g (eV)	E_{VBM} (eV)	E_{CBM} (eV)	Bandgap Type
$MoSe_2$	2.02	−5.63	−3.61	Direct
HfS_2	1.99	−6.93	−4.94	Indirect
$MoSe_2/HfS_2$	0.53	−5.69	−5.16	Direct
$MoSe_2/HfS_2$ with −6% strain	0.53	−5.69	−5.16	Direct
$MoSe_2/HfS_2$ with −3% strain	0.54	−5.70	−5.16	Direct
$MoSe_2/HfS_2$ with 3% strain	0.53	−5.69	−5.16	Direct
$MoSe_2/HfS_2$ with 6% strain	0.53	−5.69	−5.16	Direct

Meanwhile, the VBM of the HfS_2 single layer was able to stride over the standard oxidation potential for O_2/H_2O, whereas the CBM was 0.5 eV lower than the standard reduction potential for H^+/H_2. So, the HfS_2 monolayer can only be used for OER. At the same time, the VBM of the $MoSe_2$ monolayer was 0.04 eV higher than the standard oxidation potential, while the CBM could straddle the standard reduction potential, indicating that the $MoSe_2$ single layer can only be applied for HER. Thus, by combining the $MoSe_2$ and HfS_2 single layers, the $MoSe_2/HfS_2$ nanocomposite can be used for photocatalytic overall water splitting. As depicted in Figure 2, the $MoSe_2/HfS_2$ heterostructure is a semiconductor with a direct bandgap of 0.53 eV, which is less than those of the individual $MoSe_2$ (2.02 eV) and HfS_2 (1.99 eV) single layers, indicating that this heterojunction can make the best of visible light and even enlarge the applied range of light to infrared light. As shown in the picture of the projected band structure, the VBM of this heterostructure is mainly composed of the $MoSe_2$ layer, while the CBM is primarily made up of the HfS_2 layer, which is in support of the separation of the photoinduced carriers.

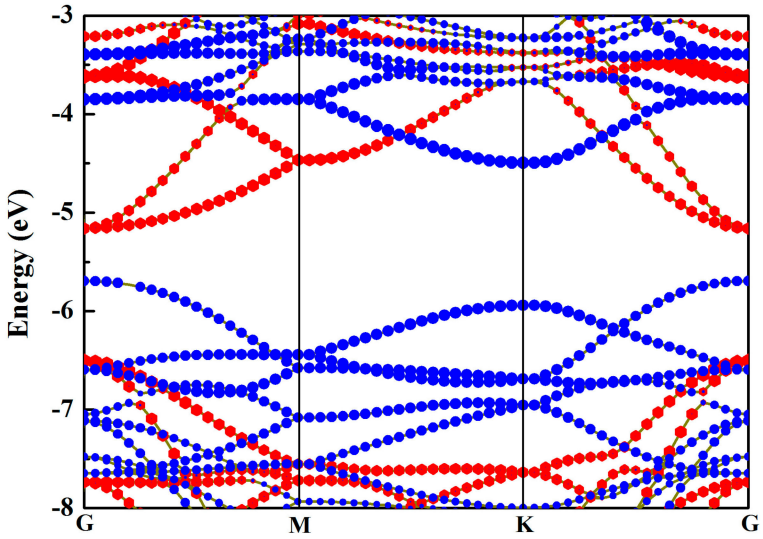

Figure 2. Projected band structure of the $MoSe_2/HfS_2$ heterostructure. The red hexagons and blue balls represent the energy bands of the HfS_2 and $MoSe_2$ layers, respectively.

In order to systematically study the photocatalytic ability of the $MoSe_2/HfS_2$ heterostructure, we employed a density of states (DOS) analysis. TDOS and PDOS represent the total and partial DOS, respectively. As displayed in Figure 3, the VBM of this heterojunction chiefly consisted of the Mo 4d and Se 4p states, which were derived from the $MoSe_2$ layer. However, the CBM was primarily made up of the Hf 5d and S 3p orbitals, which were rooted in the HfS_2 slab. Thus, the VBM and CBM of this heterojunction were separated into different layers, which is consistent with the previous analysis about the band structure.

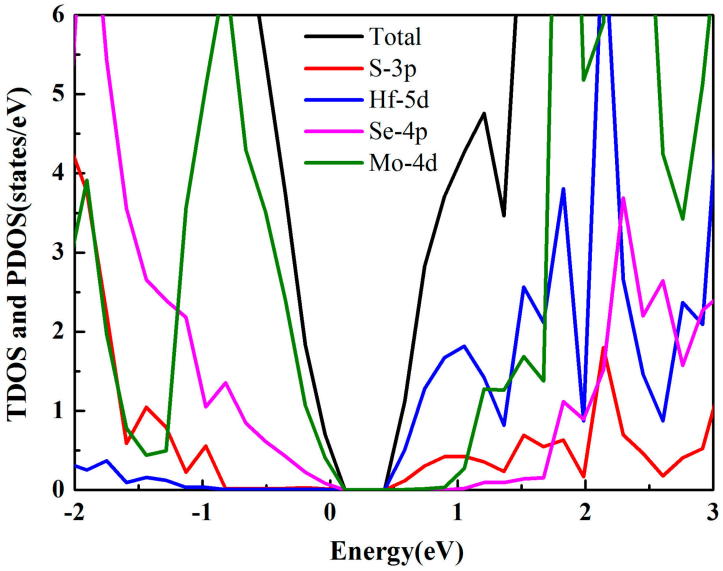

Figure 3. Total and partial density of states of the $MoSe_2/HfS_2$ nanocomposite.

The effective separation of the photo-generated electron–hole pairs is an essential factor for improving the photocatalytic activity. Thus, we applied the charge density difference and Bader charge analysis to investigate the carrier migrating processes. The charge density differences of this heterostructure are defined as this: $\triangle\varrho = \varrho_{MoSe2/HfS2} - \varrho_{MoSe2} - \varrho_{HfS2}$, where $\varrho_{MoSe2/HfS2}$, ϱ_{MoSe2}, and ϱ_{HfS2} indicate the charge density of the $MoSe_2/HfS_2$ nanocomposite, freestanding $MoSe_2$, and HfS_2 nanosheets, respectively. The small bandgap (0.53 eV) in this heterostructure was favorable to enhancing the interlayer carrier transfer. As depicted in Figure 4, there is obvious charge accumulation and depletion near the interface. The $MoSe_2$ layer was apt to lose charge, while the HfS_2 slab tended to gain charge. Hence, the charge transfer between two layers brought about an internal electric field pointing from the $MoSe_2$ layer to the HfS_2 slab, which is in accordance with the previous report that the electric field generally points from the hydrogen evolution catalyst to the oxygen evolution catalyst [25]. In order to evaluate the quantity of charge transfer, we employed the Bader charge analysis. The S and Se atoms were liable to acquire electrons, while the Hf and Mo atoms were apt to lose electrons. As a whole, the migrated electrons from the $MoSe_2$ layer to the HfS_2 slab were 0.052 e, which is in keeping with the charge density differences analysis.

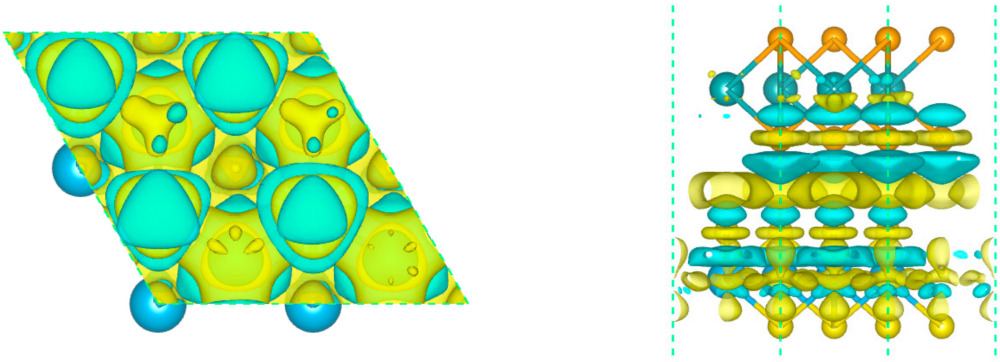

(**a**) (**b**)

Figure 4. Electron density difference in the $MoSe_2/HfS_2$ nanocomposite with an isovalue of 0.0001 e/Å^3. Yellow and cyan areas represent accumulation and depletion, respectively. Charge density differences for the $MoSe_2/HfS_2$ heterojunction (top view (**a**) and side view(**b**)).

After the light irradiation, the electrons on the VB of $MoSe_2$ and HfS_2 slabs were excited to the CB of these layers. The internal electric field of the $MoSe_2/HfS_2$ nanocomposite was in favor of the electron migration from the CB of HfS_2 to the VB of $MoSe_2$. Meanwhile, the electric field hindered the electron transfer from the CB of $MoSe_2$ to the CB of HfS_2 and the hole transfer from the VB of HfS_2 to the VB of $MoSe_2$. Moreover, because the CBM of HfS_2 and VBM of $MoSe_2$ were close to each other (0.69 eV)—as displayed in Table 1—the photogenerated electrons in the CBM of HfS_2 layer could easily recombine with the holes in the VBM of the $MoSe_2$ layer. Finally, the photoinduced electrons in the CBM of $MoSe_2$ slab and the holes in the VBM of HfS_2 slab could both be preserved, which enabled the $MoSe_2/HfS_2$ nanocomposite to possess high redox ability. The schematic illustration of the Z-scheme photocatalytic mechanism for the $MoSe_2/HfS_2$ nanocomposite is illustrated in Figure 5. Therefore, in comparison with the $MoSe_2$ and HfS_2 monolayers, the $MoSe_2/HfS_2$ heterostructure can improve the separation efficiency of the photogenerated carriers and enhance the redox ability.

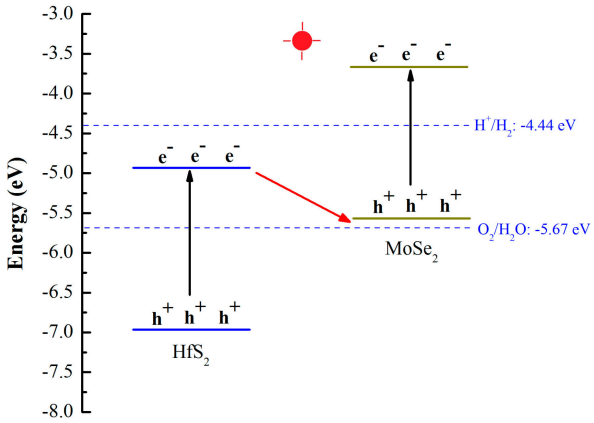

Figure 5. The schematic illustration of the Z-scheme photocatalytic mechanism for the $MoSe_2/HfS_2$ nanocomposite.

In addition, stress is inevitable in industrial production and may also originate from the mismatch of the lattices between different materials. Thus, we investigated the band edge positions of the $MoSe_2/HfS_2$ nanocomposite as a function of in-plain strains. By applying the strains in the range from −6% to 6%, the calculated band edge positions of the $MoSe_2/HfS_2$ heterostructure remained almost unchanged, as displayed in Figure 6. Thus, the band structures of $MoSe_2/HfS_2$ heterostructure are stable, which is different from the typical type II heterojunctions [11,15]. Therefore, the stable electronic property is in favor of future industrial applications.

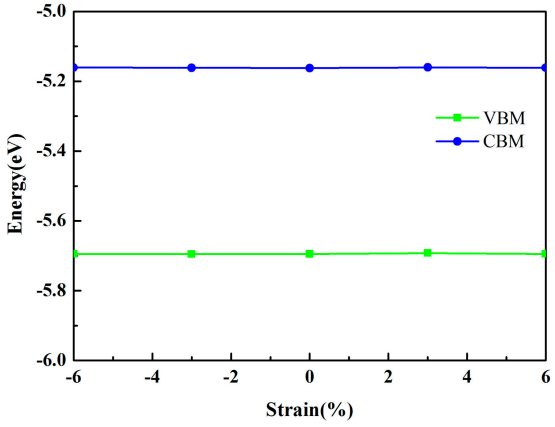

Figure 6. The band edge positions of the $MoSe_2/HfS_2$ nanocomposite as a function of in-plain strains.

3.3. Optical Properties

Optical absorption spectra are able to directly characterize the catalytic performance of photocatalysts. In this work, we employed the VASPKIT software to analyze the optical absorption properties. The optical absorption coefficient $I(\omega)$ can be acquired from the dynamical dielectric response function $\varepsilon(\omega)$, which can be expressed by this equation: $I(\omega) = \sqrt{2}\omega[\sqrt{\varepsilon_1(\omega)^2 + \varepsilon_2(\omega)^2} - \varepsilon_1(\omega)]^{\frac{1}{2}}$. Compared with those of the HfS_2 and $MoSe_2$ monolayers, the optical absorption intensity of the $MoSe_2/HfS_2$ heterostructure is strengthened, especially in the visible and infrared region, as shown in Figure 7. Because the HfS_2 single layer is an indirect semiconductor, the enhancement of the optical absorption mainly stems from the $MoSe_2$ monolayer, which possesses a direct bandgap. Moreover, the evident red shift in this nanocomposite is mainly derived from the transition from the S 3p state to the Se 4p state. Furthermore, there are obvious absorption peaks even at 400 and 600 nm. Therefore, the $MoSe_2/HfS_2$ can take full advantage of the visible light.

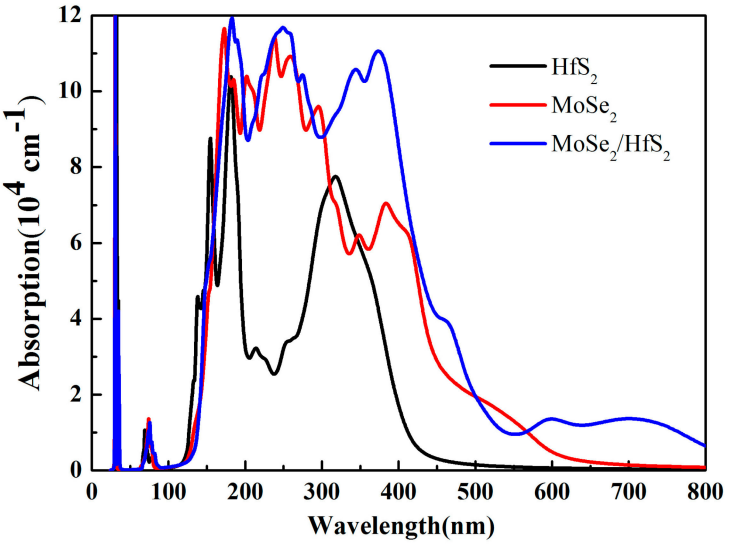

Figure 7. Optical absorption spectra of the related 2D materials and nanocomposite.

4. Conclusions

To summarize, we have designed a $MoSe_2/HfS_2$ bilayer heterostructure and investigated its electronic and optical properties according to the direct Z-scheme mechanism by employing the hybrid density functional theory. The computed results reveal that the HfS_2 monolayer and $MoSe_2$ single layer can only be used for OER and HER, respectively. By combining the $MoSe_2$ and HfS_2 monolayers, the $MoSe_2/HfS_2$ nanocomposite, which is a direct Z-scheme photocatalyst, can be used for photocatalytic overall water splitting. As depicted in the projected band structure, the VBM of this heterostructure is mainly composed of the $MoSe_2$ layer, while the CBM is primarily made up of the HfS_2 layer. By applying the charge density difference and Bader charge analyses, the charge transfer between two layers brought about a built-in electric field pointing from the $MoSe_2$ layer to the HfS_2 slab, which is in support of the separation of the photoinduced carriers. Moreover, the photogenerated electrons in the CBM of the $MoSe_2$ slab and the holes in the VBM of the HfS_2 slab can both be preserved, which enables the $MoSe_2/HfS_2$ nanocomposite to possess high redox ability. When strains are applied to the $MoSe_2/HfS_2$ heterostructure, the band structures of this heterostructure are stable, which is in favor of future industrial applications. Compared with those of HfS_2 and $MoSe_2$ monolayers, the optical absorption intensity of the $MoSe_2/HfS_2$ heterostructure is distinctly strengthened in the visible and infrared region. Therefore, the $MoSe_2/HfS_2$ heterojunction is a potential direct Z-scheme photocatalyst for photocatalytic overall water splitting. This work may provide an effective route for developments in clean and renewable energy.

Author Contributions: The study was proposed and planned by H.C. The calculations were carried out by B.W., X.W., P.W., T.Y., H.Y., and G.W. discussed the results, B.W. wrote the manuscript.

Funding: This work has been financially supported by the National Natural Science Foundation of China (Grant Nos.11875226 and 11874306), the Natural Science Foundation of Chongqing (Grant No. CSTC-2017jcyjBX0035), the Fundamental Research Funds for the Central Universities (Grant Nos. XDJK2017C062 and XDJK2017B020), and the educational reform Research Funds of Southwest Universities (Grant No. 2018JY0730).

Acknowledgments: Biao Wang thanks Anlong Kuang and Junli Chang (from Southwest University) for their help in this work.

Conflicts of Interest: The authors declare no conflict of interest.

References

1. Miseki, Y.; Sayama, K. Photocatalytic Water Splitting for Solar Hydrogen Production Using the Carbonate Effect and the Z-Scheme Reaction. *Adv. Energy Mater.* **2018**, 1801294. [CrossRef]
2. Fujishima, A.; Honda, K. Electrochemical photolysis of water at a semiconductor electrode. *Nature* **1972**, *238*, 37–38. [CrossRef] [PubMed]
3. Eshete, Y.A.; Ling, N.; Kim, S.; Kim, D.; Hwang, G.; Cho, S.; Yang, H. Vertical Heterophase for Electrical, Electrochemical, and Mechanical Manipulations of Layered $MoTe_2$. *Adv. Funct. Mater.* **2019**, 1904504. [CrossRef]
4. Bonaccorso, F.; Colombo, L.; Yu, G.; Stoller, M.; Tozzini, V.; Ferrari, A.; Ruoff, R.; Pellegrini, V. Graphene, related two-dimensional crystals, and hybrid systems for energy conversion and storage. *Science* **2015**, *347*, 41–51. [CrossRef]
5. Fan, X.; Yang, Y.; Xiao, P.; Lau, W. Site-specific catalytic activity in exfoliated MoS_2 single-layer polytypes for hydrogen evolution: Basal plane and edges. *J. Mater. Chem. A* **2014**, *2*, 20545–20551. [CrossRef]
6. Singh, A.; Mathew, K.; Zhuang, H.; Hennig, R. Computational screening of 2D materials for photocatalysis. *J. Phys. Chem. Lett.* **2015**, *6*, 1087–1098. [CrossRef]
7. Zhu, W.; Qiu, X.; Iancu, V.; Chen, X.; Pan, H.; Wang, W.; Dimitrijevic, N.M.; Rajh, T.; Meyer, H.M.; Paranthaman, M.P.; et al. Band gap narrowing of titanium oxide semiconductors by noncompensated anion-cation codoping for enhanced visible-light photoactivity. *Phys. Rev. Lett.* **2009**, *103*, 226401. [CrossRef]
8. Wang, H.L.; Zhang, L.S.; Chen, Z.G.; Hu, J.Q.; Li, S.J.; Wang, Z.H.; Liu, J.S.; Wang, X.C. Semiconductor heterojunction photocatalysts: Design, construction, and photocatalytic performances. *Chem. Soc. Rev.* **2014**, *43*, 5234–5244. [CrossRef]
9. Formal, F.L.; Pendlebury, S.R.; Cornuz, M.; Tilley, S.D.; Gratzel, M.; Durrant, J.R. Back electron-hole recombination in hematite photoanodes for water splitting. *J. Am. Chem. Soc.* **2014**, *136*, 2564–2574. [CrossRef]
10. Deng, D.H.; Novoselov, K.S.; Fu, Q.; Zheng, N.F.; Tian, Z.Q.; Bao, X.H. catalysis with two-dimensional materials and their heterostructures. *Nat. Nanotechnol.* **2016**, *11*, 218–230. [CrossRef]
11. Zhang, X.; Meng, Z.; Rao, D.; Wang, Y.; Shi, Q.; Liu, Y.; Wu, H.; Deng, K.; Liu, H.; Lu, R. Efficient band structure tuning, charge separation, and visible-light response in ZrS_2-based van der Waals heterostructures. *Energ. Environ. Sci.* **2016**, *9*, 841–849. [CrossRef]
12. Zhang, C.H.; Zhao, S.L.; Jin, C.H.; Koh, A.L.; Zhou, Y.; Xu, W.G.; Li, Q.C.; Xiong, Q.H.; Peng, H.L.; Liu, Z.F. Direct growth of large-area graphene and boron nitride heterostructures by a co-segregation method. *Nature Commun.* **2015**, *6*, 6519. [CrossRef] [PubMed]
13. Kang, J.; Tongay, S.; Zhou, J.; Li, J.B.; Wu, J.Q. Band offsets and heterostructures of two-dimensional semiconductors. *Appl. Phys. Lett.* **2013**, *102*, 012111. [CrossRef]
14. Ling, F.; Kang, W.; Jing, H.; Zeng, W.; Chen, Y.; Liu, X.; Zhang, Y.; Qi, L.; Fang, L.; Zhou, M. Enhancing hydrogen evolution on the basal plane of transition metal dichacolgenide van der Waals heterostructures. *NPJ Comput. Mater.* **2019**, *5*, 20. [CrossRef]
15. Wang, B.; Yuan, H.K.; Chang, J.L.; Chen, X.R.; Chen, H. Two dimensional $InSe/C_2N$ van der Waals heterojunction as enhanced visible-light responsible photocatalyst for water splitting. *Appl. Surf. Sci.* **2019**, *485*, 375–380. [CrossRef]
16. Bard, A.J. Photoelectrochemistry and heterogeneous photo-catalysis at semiconductors. *J. Photochem.* **1979**, *10*, 59–75. [CrossRef]

17. Pan, Z.M.; Zhang, G.G.; Wang, X.C. Polymeric Carbon Nitride/RGO/Fe_2O_3: All Solid State Z-Scheme System for Photocatalytic Overall Water Splitting. *Angew. Chem. Int. Ed.* **2019**, *58*, 7102–7106. [CrossRef]
18. Fu, C.F.; Luo, Q.Q.; Liao, X.X.; Yang, J.L. Two-dimensional van der waals nanocomposites as z-scheme type photocatalysts for hydrogen production from overall water splitting. *J. Mater. Chem. A* **2016**, *4*, 18892–18898. [CrossRef]
19. Maeda, K. Z-scheme water splitting using two different semiconductor photocatalysts. *ACS Catal.* **2013**, *3*, 1486–1503. [CrossRef]
20. Zhou, P.; Yu, J.G.; Jaroniec, M. All-solid-state z-scheme photocatalytic systems. *Adv. Mater.* **2014**, *26*, 4920–4935. [CrossRef]
21. Li, J.Q.; Yuan, H.; Zhu, Z.F. Artificial photosynthetic z-scheme photocatalyst for hydrogen evolution with high quantum efficiencys. *J. Mol. Catal. A Chem.* **2015**, *410*, 133–139. [CrossRef]
22. Wang, L.; Zheng, X.S.; Chen, L.; Xiong, Y.J.; Xu, H.X. Van der waals heterostructures comprised of ultrathin polymer nanosheets for efficient z scheme overall water splitting. *Angew. Chem. Int. Ed.* **2018**, *57*, 3454–3458. [CrossRef] [PubMed]
23. Guo, H.L.; Du, H.; Jiang, Y.F.; Jiang, N.; Shen, C.C.; Zhou, X.; Liu, Y.N.; Xu, A.W. Artificial photosynthetic z-scheme photocatalyst for hydrogen evolution with high quantum efficiencys. *J. Phys. Chem. C* **2017**, *121*, 107–114. [CrossRef]
24. Fan, Y.C.; Yang, B.; Song, X.H.; Shao, X.F.; Zhao, M.W. Direct z–scheme photocatalytic overall water splitting on 2D CdS/InSe heterostructures. *J. Phys. D Appl. Phys.* **2018**, *51*, 395501. [CrossRef]
25. Fu, C.F.; Zhang, R.Q.; Luo, Q.Q.; Li, X.X.; Yang, J.L. Construction of Direct Z-Scheme Photocatalysts for Overall Water Splitting Using Two-Dimensional van der Waals Heterojunctions of Metal Dichalcogenides. *J. Comput. Chem.* **2019**, *40*, 980–987. [CrossRef]
26. Ju, L.; Dai, Y.; Wei, W.; Li, M.M.; Huang, B.B. DFT investigation on two-dimensional GeS/WS_2 van der Waals heterostructure for direct Z-scheme photocatalytic overall water splitting. *Appl. Surf. Sci.* **2018**, *434*, 365–374. [CrossRef]
27. Li, H.; Tu, W.; Zhou, Y.; Zou, Z. Z-scheme photocatalytic systems for promoting photocatalytic performance: Recent progress and future challenges. *Adv. Sci.* **2016**, *31*, 500389. [CrossRef]
28. Di, T.M.; Zhu, B.C.; Cheng, B.; Yu, J.G.; Xu, J.S. A direct Z-scheme g-C_3N_4/SnS_2 photocatalyst with superior visible-light CO_2 reduction performance. *J. Catal.* **2017**, *352*, 532–541. [CrossRef]
29. Meng, A.Y.; Zhu, B.C.; Zhong, B.; Zhang, L.Y.; Cheng, B. Direct Z-scheme TiO_2/CdS hierarchical photocatalyst for enhanced photocatalytic H_2-production activity. *Appl. Surf. Sci.* **2017**, *422*, 518–527. [CrossRef]
30. Liu, F.L.; Shi, R.; Wang, Z.; Weng, Y.X.; Che, C.M.; Chen, Y. Direct z scheme hetero-phase junction of black/red phosphorus for photocatalytic water splitting. *Angew. Chem. Int. Ed.* **2019**, *58*, 11791–11795. [CrossRef]
31. Zhang, W.J.; Hu, Y.; Yan, C.Z.; Hong, D.C.; Chen, R.P.; Xue, X.L.; Yang, S.Y.; Tian, Y.X.; Tie, Z.X.; Jin, Z. Surface plasmon resonance enhanced direct Z-scheme TiO_2/ZnTe/Au nanocorncob heterojunctions for efficient photocatalytic overall water splitting. *Nanoscale* **2019**, *11*, 9053–9060. [CrossRef] [PubMed]
32. Wang, Q.; Hisatomi, T.; Jia, Q.; Tokudome, H.; Zhong, M.; Wang, C.; Pan, Z.; Takata, K.; Nakabayashi, M.; Shibata, N.; et al. Scalable water splitting on particulate photocatalyst sheets with a solar-to-hydrogen energy conversion eciency exceeding 1%. *Nat. Mater.* **2016**, *15*, 611–615. [CrossRef] [PubMed]
33. Novoselov, K.; Geim, A.; Morozov, S.; Jiang, D.; Zhang, Y.; Dubonos, S.; Grigorieva, I.; Firsov, A. Electric field effect in atomically thin carbon films. *Science* **2004**, *306*, 666–669. [CrossRef] [PubMed]
34. Zhao, Z.W.; Sun, Y.J.; Dong, F. Graphitic carbon nitride based nanocomposites: A review. *Nanoscale* **2015**, *7*, 15–37. [CrossRef]
35. Coleman, J.N.; Lotya, M.; O'Neill, A.; Bergin, S.D.; King, P.J.; Khan, U.; Young, K.; Gaucher, A.; De, S.; Smith, R.J. Two-dimensional nanosheets produced by liquid exfoliation of layered materials. *Science* **2011**, *331*, 568–571. [CrossRef]
36. Singh, D.; Gupta, S.K.; Sonvane, Y.; Kumarc, A.; Ahujad, R. 2D-HfS_2 as an efficient photocatalyst for water splitting. *Catal. Sci. Technol.* **2016**, *6*, 6605–6614. [CrossRef]
37. Zhang, H. Ultrathin two-dimensional nanomaterials. *ACS Nano* **2015**, *9*, 9451–9469. [CrossRef]
38. Novoselov, K.S.; Mishchenko, A.; Carvalho, A.; Neto, A.H.C. 2D materials and van der Waals heterostructures. *Science* **2016**, *353*, 461–473. [CrossRef]
39. Zhuang, H.; Hennig, R. Theoretical perspective of photocatalytic properties of single-layer SnS_2. *Phys. Rev. B* **2013**, *88*, 115314. [CrossRef]
40. Zhuang, H.; Hennig, R. Single-layer group-III monochalcogenide photocatalysts for water splitting. *Chem. Mater.* **2013**, *25*, 3232–3238. [CrossRef]

41. Yi, J.J.; Li, H.P.; Gong, Y.J.; She, X.J.; Song, Y.H.; Xu, Y.G.; Deng, J.J.; Yuan, S.Q.; Xu, H.; Li, H.M. Phase and interlayer effect of transition metal dichalcogenide cocatalyst toward photocatalytic hydrogen evolution: The case of $MoSe_2$. *Appl. Cata. B Environ.* **2019**, *243*, 330–336. [CrossRef]
42. Zhu, J.D.; Xu, S.R.; Ning, J.; Wang, D.; Zhang, J.C.; Hao, Y. Gate-Tunable Electronic Structure of Black Phosphorus/HfS_2 P−N van der Waals Heterostructure with Uniformly Anisotropic Band Dispersion. *J. Phys. Chem. C* **2017**, *121*, 24845–24852. [CrossRef]
43. Xu, Y.; Zhao, W.; Xu, R.; Shi, Y.; Zhang, B. Synthesis of ultrathin CdS nanosheets as efficient visible-light-driven water splitting photocatalysts for hydrogen evolution. *Chem. Commun.* **2013**, *49*, 9803–9805. [CrossRef] [PubMed]
44. Wang, B.; Kuang, A.L.; Luo, X.K.; Wang, G.Z.; Yuan, H.K.; Chen, H. Bandgap engineering and charge separation in two-dimensional GaS-based van der Waals heterostructures for photocatalytic water splitting. *Appl. Surf. Sci.* **2018**, *439*, 374–379. [CrossRef]
45. Kresse, G.; Furthmüller, J. Efficient iterative schemes for ab initio total energy calculations using a plane-wave basis set. *Phys. Rev. B* **1996**, *54*, 11169–11186. [CrossRef]
46. Kresse, G.; Joubert, D. From ultrasoft pseudopotentials to the projector augmented-wave method. *Phys. Rev. B* **1999**, *59*, 1758–1775. [CrossRef]
47. Blöchl, P.E. Projector augmented wave method. *Phys. Rev. B* **1994**, *540*, 17953–17979. [CrossRef]
48. White, J.A.; Bird, D.M. Implementation of gradient-corrected exchange correlation potentials in Car-Parrinello total-energy calculations. *Phys. Rev. B* **1994**, *50*, 4954–4957. [CrossRef]
49. Ernzerhof, M.; Scuseria, G.E. Assessment of the Perdew-Burke-Ernzerh of exchange-correlation functional. *J. Chem. Phys.* **1999**, *110*, 5029–5036. [CrossRef]
50. Bengtsson, L. Dipole correction for surface supercell calculations. *Phys. Rev. B* **1999**, *50*, 12301. [CrossRef]
51. Heyd, J.; Scuseria, G.E. Hybrid functionals based on a screened Coulomb potential. *J. Chem. Phys.* **2003**, *118*, 8207–8215. [CrossRef]
52. Grimme, S.; Antony, J.; Ehrlich, S.; Krieg, S. A consistent and accurate ab initio parametrization of density functional dispersion correction (DFT-D) for the 94 elements H-Pu. *J. Chem. Phys.* **2010**, *132*, 154104. [CrossRef] [PubMed]
53. Monkhorst, H.J.; Pack, J.D. Special points for Brillouin-zone integrations. *Phys. Rev. B* **1976**, *13*, 5188–5192. [CrossRef]
54. Ramasubramaniam, A. Large excitonic effects in monolayers of molybdenum and tungsten dichalcogenides. *Phys. Rev. B* **2012**, *86*, 115409. [CrossRef]